SUPPLEMENTAL INFORMATION

Modelling heteroFRET efficiencies from the bent and extended fusion protein models of mRFP-IgEFc-eGFP

(a) Basic principles

Prior to describing how the FRET (Förster resonance energy transfer) efficiency was calculated across the different biosensor models, the different parameters of Förster theory (see Ref. 45 in the main text) which determine the efficiency are introduced and discussed. From a photophysical perspective, the FRET efficiency, E, is the probability that when a photon excites a donor fluorophore from its ground state to an excited state, the excited-state of the donor transfers its energy non-radiatively to the acceptor, rather than decaying back to the ground state radiatively (i.e., with the release of a photon) or otherwise non-radiatively (radiationless transition, e.g., internal conversion, collisional quenching, intersystem crossing to a triplet state, bleaching) as shown in equation S1:

$$E = \frac{k_T}{\frac{1}{\tau_{0D}} + k_T} \qquad \text{(Eq. S1)}$$

where k_T is the rate constant for the FRET process and $1/\tau_{0D}$ is the rate constant (i.e., inverse excited-state lifetime) for the sum of the radiative and non-radiative decay rates of the donor excited-state to the ground state in the absence of acceptor.

The major application of FRET to the biological sciences is through its use as a molecular measuring stick. This arises from the acute inverse sixth-power distance dependence of FRET: $k_T = \frac{1}{\tau_{0D}}\left(\frac{R_0}{R}\right)^6$, where R_0 is the Förster distance for a given donor-acceptor pair, which is equal to the inter-fluorophore distance for which the FRET is 50% efficient, and typically has values on the scale of biological macromolecules (i.e., 1-10 nm) – the energy transfer efficiency diminishes steeply the further the donor and acceptor fluorophores are apart. On substitution of the above definition of k_T into equation S1, the dependence of FRET efficiency, E, on the separation, R, between the two fluorophores is thus seen to be defined as shown in equation S2:

$$E = \frac{(R_0/R)^6}{1 + (R_0/R)^6} = \frac{R_0^6}{R^6 + R_0^6} \qquad \text{(Eq. S2)}$$

This apparently simplistic usage of the FRET efficiency, as a tool to measure distances, is compromised by the complication that inter-fluorophore separation is not the only physical parameter of the donor and acceptor that contributes to defining the FRET efficiency, E. Specifically, the relative orientations of the electronic transition dipoles in the donor and acceptor fluorophores to each other, and to the separation vector, affect the efficiency with which the FRET occurs through the orientation factor, κ^2, which modulates the value of R_0 for the observed orientation as shown in equation S3:

$$R_0^6 = \frac{9Q_0(\ln 10)\kappa^2 J}{128\pi^5 n^4 N_A'} \qquad \text{(Eq. S3)}$$

where Q_0 is the quantum yield of the donor in the absence of acceptor, n is the refractive index of the medium, N_A' is Avogadro's constant per mmole, and J is the overlap integral calculated from the donor emission and acceptor absorption spectra as shown in equation S4:

$$J = \frac{\int_0^\infty \varepsilon_A(\lambda) F_D(\lambda) \lambda^4 d\lambda}{\int_0^\infty F_D(\lambda) d\lambda} \qquad \text{(Eq. S4)}$$

where $\varepsilon_A(\lambda)$ is the molar extinction coefficient at the wavelength λ, and $F_D(\lambda)$ is the arbitrarily scaled donor emission spectrum (intensity per unit wavelength at wavelength λ). Employing the usual units of extinction coefficient (cm^2/mmole) and defining wavelength in nm leads to $R_0^6 = 8.784 \times 10^{-11}(Q_0\kappa^2 Jn^{-4})$ nm^6 and thereby to $R_0 = 0.02108\sqrt[6]{Q_0\kappa^2 Jn^{-4}}$ nm.

The orientation factor, κ^2, varies between values of 0 and 4. However, for the specific case where both the donor and acceptor adopt dynamic random 3-D orientations with respect to the separation vector, it has a dynamic random isotropic value of 2/3 (see Refs. 44, 45, 51 and 52 in the main text). A common simplifying assumption found in the literature is that 2/3 can be taken for κ^2 *in lieu* of its actual value. Leaving aside the special chance cases in which the 2/3 value applies specifically, this assumption is problematic in that it strictly applies only to the scenario in which (a) the orientational distributions of both donor and acceptor with respect to the separation vector are isotropic or pseudo-isotropic, and (b) the rate constants describing independent random isotropic (or pseudo-isotropic) rotations of the fluorophores (not their mutual rotation, i.e., the rotation of the separation vector, such as would be the case for donor and acceptor moieties making up part of the structure of a small molecule rotating rapidly in solution) are very much greater than the rate constant for donor decay. In this case, during the time it takes for the donor decay to occur, the fluorophores will have independently visited a large number of these different random orientations, so that the FRET efficiency is essentially that for a dynamic random isotropic average orientation factor. In the following, it will be assumed that, as in the normal convention, R_0^6 contains the 2/3 average, and the actual orientation factor will appear separately from it (with a multiplying factor of 3/2 to allow for the included 2/3 average value). The orientation factor dependency needs to be taken explicitly into account when the rate constant for donor decay is very much greater than one or both of the rotational constants. Such a scenario occurs where GFP and/or related proteins take up either one or – as in the present study – both, donor and acceptor roles, since the fluorophore is contained within an ~226 residue barrel and thus rotates significantly more slowly than the donor excited-state decays, even when it is not rigidly attached to a larger protein. However, at least in the present case of IgEFc containing donor (eGFP) and acceptor (mRFP) constructs, where slow rotational exchange between a large number of relatively stable conformers occurs, the FRET system will comprise a population of static conformers each with not only its own particular orientation factor, κ^2, which will be defined in the following section, but also separation, R. Hence the average FRET efficiency, $\langle E \rangle$, is a static average with respect to both orientation factor and separations, made up of individual efficiencies for each of the N conformers i, using equation S5:

$$\langle E \rangle = \frac{1}{N}\sum_{i=1}^{N} \frac{\frac{3}{2}\kappa_i^2 \left(\frac{R_0}{R}\right)^6}{1+\frac{3}{2}\kappa_i^2 \left(\frac{R_0}{R}\right)^6} = \frac{1}{N}\sum_{i=1}^{N} \frac{\frac{3}{2}\kappa_i^2 R_0^6}{R^6+\frac{3}{2}\kappa_i^2 R_0^6} \qquad \text{(Eq. S5)}$$

(b) Calculation of the heteroFRET efficiencies for each of the 1300 modelled conformers, i

Since use of the dynamic random isotropic average κ^2 was not appropriate in the present context, the FRET efficiency for each of the 1300 models of the mRFP-IgEFc-eGFP biosensor was instead determined using values of R and κ^2 calculated from the models. In modelling the biosensor the GFP fluorophore was used to represent the C-terminal donor eGFPs as well as a surrogate for the N-terminal acceptor mRFPs, as the fluorophore transition dipole orientation is better defined for eGFP. An outline chemical structure of the GFP fluorophore, 4-(*p*-hydoxybenzylidene)imidazole-5-one, is shown in the diagram below.

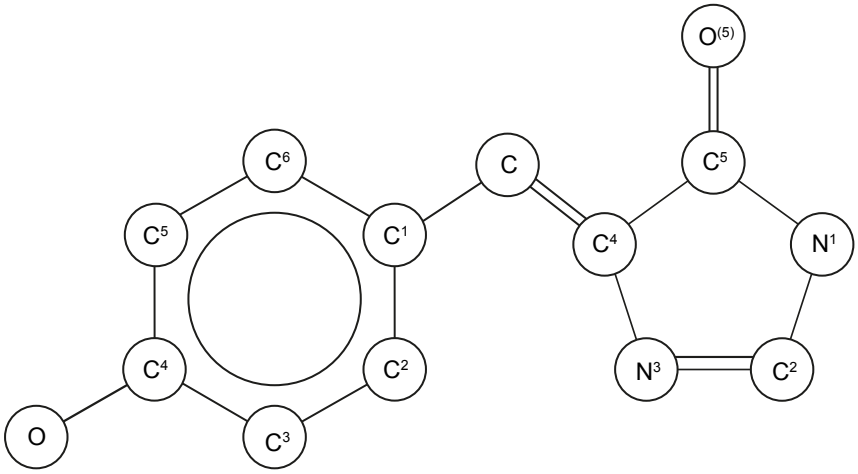

The chemical structure of the GFP fluorophore, 4-(*p*-hydoxybenzylidene)imidazole-5-one

Average intra- and cross-chain separation vectors **R** were calculated for each of the stable 1300 modelled conformers as the average of four vectors linking the coordinates of the donor and acceptor surrogate GFP benzylidene C^1 and C^2 and imidazolone N^3 and C^4 atoms within the fluorophores. In each case, the average donor-acceptor separation, R, was defined as being the length (i.e., the modulus, $|\mathbf{R}|$) of the average vector **R**. The transition moments of the donor and acceptor fluorophores are represented by the vectors **D** and **A**, respectively, and were calculated for each conformation as the average of those obtained from the coordinates of the benzylidene C^6 and imidazolone O^5 and those of the benzylidene C^3 and imidazolone N^1 atoms (see Refs. 36 and 43 in the main text). The orientation factor, κ^2, was calculated using the relationship linking the angles between vectors **D**, **A**, and **R** as shown in equation S6 (see Refs. 44, 45 and 50 in the main text):

$$\kappa^2 = (\cos\theta_T - 3\cos\theta_D \cos\theta_A)^2 \qquad \text{(Eq. S6)}$$

where θ_T is the angle between vectors **D** and **A**, θ_D is the angle between vectors **D** and **R**, and θ_A that between vectors **A** and **R**. Each cosine in equation S6 was defined from the two vectors subtending the relevant angle, via the dot product of their unit vectors (i.e., vector divided by its modulus), e.g. θ_T via $\widehat{\mathbf{D}}$ and $\widehat{\mathbf{A}}$, as shown in equation S7:

$$\cos\theta_T = \widehat{\mathbf{D}} \cdot \widehat{\mathbf{A}} \qquad \text{(Eq. S7)}$$

Equivalent calculations were carried out for $\cos\theta_D$ and $\cos\theta_A$, and the κ^2 for each donor-acceptor pair obtained by substitution into equation S6. The orientation factors may also be calculated more directly by substitution of the modulated vector dot products into equation S6 for the cosines, as shown in equation S8:

$$\kappa^2 = \left[\left(\frac{\mathbf{D}\cdot\mathbf{A}}{|\mathbf{D}||\mathbf{A}|} - 3\left(\frac{\mathbf{D}\cdot\mathbf{R}}{|\mathbf{D}||\mathbf{R}|}\right)\left(\frac{\mathbf{A}\cdot\mathbf{R}}{|\mathbf{A}||\mathbf{R}|}\right)\right)\right]^2 = \left[\left(\widehat{\mathbf{D}}\cdot\widehat{\mathbf{A}}\right) - 3\left(\widehat{\mathbf{D}}\cdot\widehat{\mathbf{R}}\right)\left(\widehat{\mathbf{A}}\cdot\widehat{\mathbf{R}}\right)\right]^2 \qquad \text{(Eq. S8)}$$

In the original publication on which the modelling is based (see Ref. 37 in the main text), an alternative version of calculating κ^2 was used, as presented in equation S9, which involves defining the plane containing **D** and **R,** together with that containing **A** and **R**, in each case to obtain the angle between them, i.e., the azimuth φ:

$$\kappa^2 = (\sin\theta_D \sin\theta_A \cos\varphi - 2\cos\theta_D \cos\theta_A)^2 \qquad \text{(Eq. S9)}$$

which arises from substitution into equation S6 for κ^2, of the completion (closure) relationship for θ_T expressed in equation S10:

$$\cos\theta_T = \sin\theta_D \sin\theta_A \cos\varphi + \cos\theta_D \cos\theta_A \qquad \text{(Eq. S10)}$$

In addition to being more computationally cumbersome, there is the disadvantage in this approach of a possible ambiguity in the choice of the azimuth, i.e., φ correctly (as in the diagram below), or$(\pi-\varphi)$ incorrectly, in relation to the θ_D and θ_A as obtained from the unit vectors $\widehat{\mathbf{D}}$, $\widehat{\mathbf{A}}$ and $\widehat{\mathbf{R}}$, and thus lying in $[0 \leq \theta_D, \theta_A \leq \pi]$.

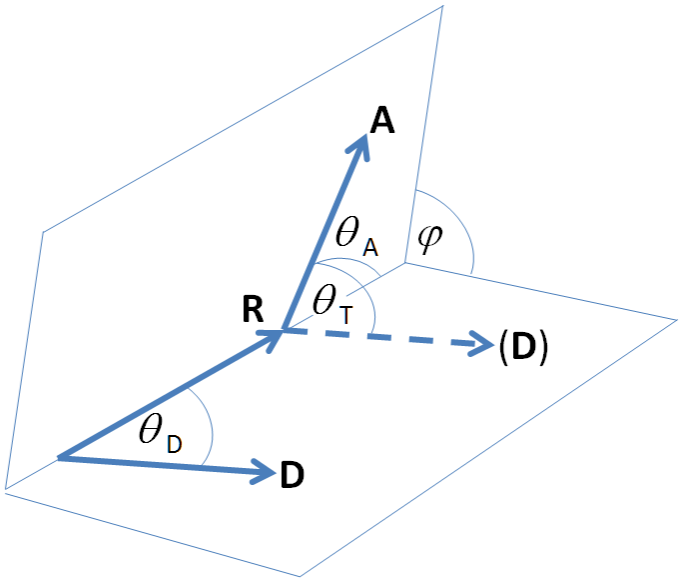

Schematic of the geometry defining the orientation factor

Considering that two donors and two acceptors are involved in each conformer (one of each on each chain "a" and "b") the relevant FRET efficiency is the average of the efficiency of transfer from each of the two donors to both of the two acceptors. The overall FRET efficiency is then the average of this over all n (1300 for both bent and extended forms) possible configurations as shown in equation S11:

$$\langle E \rangle = \frac{1}{n}\sum_{i=1}^{n}\frac{1}{2}\left[\frac{\frac{3}{2}\kappa_{aai}^2\left(\frac{R_0}{R_{aai}}\right)^6 + \frac{3}{2}\kappa_{abi}^2\left(\frac{R_0}{R_{abi}}\right)^6}{1+\frac{3}{2}\kappa_{aai}^2\left(\frac{R_0}{R_{aai}}\right)^6 + \frac{3}{2}\kappa_{abi}^2\left(\frac{R_0}{R_{abi}}\right)^6} + \frac{\frac{3}{2}\kappa_{bbi}^2\left(\frac{R_0}{R_{bbi}}\right)^6 + \frac{3}{2}\kappa_{bai}^2\left(\frac{R_0}{R_{bai}}\right)^6}{1+\frac{3}{2}\kappa_{bbi}^2\left(\frac{R_0}{R_{bbi}}\right)^6 + \frac{3}{2}\kappa_{bai}^2\left(\frac{R_0}{R_{bai}}\right)^6}\right]$$

(Eq. S11)

where $\langle E \rangle$ is the average FRET efficiency, while κ_{aai}^2, for example, is the orientation factor when the donor and acceptor are both on the "a"-chain of the ith conformer, and R_{abi}, for example, is the separation between the donor and acceptor on the "a"- and "b"-chains, respectively. As already indicated, the factors 3/2 in the relative rate constants arise from substituting the appropriate individual κ^2 values for the 2/3 value of κ^2 in the Förster R_0 value of 4.66 nm. This value is adjusted from the 4.7 nm value of Peter *et al.* (Ref. S1) using a refractive index of 1.3375 (Ref. S2) and a quantum yield of 0.64 (Ref. S3). These calculations make the approximation that, however complex the decay processes may be (see below), effective average rate constants for both the "a" and "b" chain donor decays in absence of acceptor apply. This is regardless of whether or not they are the same for the two donors "a" and "b", provided that the donors are otherwise spectroscopically identical, since they cancel out between the respective numerators and denominators of the rate forms

(compare Eq. S2 with Eq. S1) of the above equation. In fact, in view of the β-barrel structure containing the eGFP fluorophore and protecting it from direct external influences, there is no reason to suppose that they would be different. Thus, a common rate, $1/\langle\tau_{0D}\rangle$, the reciprocal of the excitation-weighted average lifetime (see Eq. 3 in main text for definition of this averaging, and Table S3 for experimental values both in presence and absence of acceptors, in both cases labeled generically as $\langle\tau\rangle$), is substituted for $1/\tau_{0D}$ in Eq. S1 above and in the definition of the FRET rate constant k_T which follows it. For the extended IgEFc configuration, this average FRET efficiency was about 0.54%, with no appreciable difference between the efficiencies contributed by each donor, and would be difficult to distinguish from zero experimentally. For the bent configuration, however, it amounted to about 9.2% (the individual donor efficiencies being very similar at about 8.9% for the "a"-chain donor and about 9.5% for the "b"-chain donor) in excellent agreement with the experimental lifetime-derived and steady-state measurements of (8.9 ± 0.7)% and (9.6 ± 0.5)%, respectively.

As indicated above, eGFP is a far from ideal donor fluorophore for quantitative studies due to its complex spectroscopic properties that cause the appearance of a biexponential donor excited-state decay even in the absence of acceptor. The origin of this behaviour (see e.g., Ref. S4, and also Refs. 29-32 in the main text) has been attributed to the existence of two excited states in exchange on the same time-scale as the excited-state decay, and/or possibly two ground states in slow exchange (or even stable equilibrium). This spectroscopic complexity is also true for the acceptor (mRFP), but in that case does not affect the energy transfer process since it is only the overall mRFP absorption spectrum (via its appearance in the overlap integral) that can affect the FRET process and hence the decay of the donor. As a consequence, both completely accurate calculation of FRET efficiencies and interpretation of experimentally determined values are not strictly possible even for a one eGFP donor-one acceptor system, let alone for the more complex two donor-two acceptor system used in the present work. Such calculations would require full information on the excited-state kinetic parameters of the donor to be available, which is not the case here.

Despite the above cautions, the validity of the experimental measurement of efficiencies is not compromised, since the definition of efficiency is the fraction of initially excited donors radiationlessly transferring their energy to acceptor(s).

(c) The effect of inter-donor homoFRET on the heteroFRET efficiencies

The present use of the equation for $\langle E\rangle$ above (equation S11) is far too simplistic since, firstly, it (a) tacitly strictly relates to donors with monoexponential excited-state decays, but assumes that this is replaceable by surrogate excitation-averaged decay times for the complex eGFP donor excited states, and (b) correspondingly uses a Förster R_0 value based on the quantum yield of the complex two-donor excited-state system. As far as these related factors are concerned, it has been assumed that the excitation-averaged donor lifetime in absence of acceptors, $\langle\tau_{0D}\rangle$, may again be taken as an approximate surrogate for the monoexponential decay time, τ_{0D}, appearing in strict FRET theory. Secondly, though, and potentially more importantly, it assumes that inter-chain homoFRET does not influence the overall average heteroFRET efficiency.

To overcome this last limitation, the long-established theory governing the kinetics of two-state excited-state systems of many kinds (see, e.g., Ref. S5: reversible excimer formation, Ref. S6: reversible energy transfer, Ref. S7: reversible heteroFRET, Ref. S8: reversible proton transfer, and Ref. S9: partition dynamics in aqueous micelle solutions) were applied, whilst tacitly retaining the

common excitation-averaged decay time $\langle\tau_{0D}\rangle$ in absence of acceptors, again as an approximate surrogate for its monoexponential form appearing in the strict theory, and invoking the limiting case applicable here that the exchange rate constants for homoFRET are identical. The average FRET efficiency, E_i, was calculated for each conformer *i*, and these values then averaged over all 1300 conformers to obtain the overall average efficiency $\langle E\rangle$. Complete sharing of excitation energy between like donors maximally increases the average donor-to-unlike acceptor heteroFRET efficiency, while partial exchange of excitation energy between like donors is also likely to have an appreciable effect on it.

In the special case of extremely rapid sharing of excitation energy between like donors, the common excitation-weighted average lifetime in absence of acceptors $\langle\tau_{0D}\rangle$ is maintained. In the presence of acceptors, but absence of donor excitation energy sharing, the corresponding two donor excited-state lifetimes, $\langle\tau_{ai}\rangle$ for the "a"-chain donor and $\langle\tau_{bi}\rangle$ for the "b"-chain donor of the *i*th conformer, are generally different due to the different dispositions of acceptors with respect to them. However, in the presence of extremely rapid FRET between donors, a new common average donor excited-state lifetime is produced, defined in general (i.e., for reversible FRET between unlike donors) by the inverse of the average rate constants for heteroFRET to the acceptors weighted by the relative rate constants for excitation energy exchange between the two donors (Ref. S10). For the case in hand, that of true homoFRET between identical donors, these relative rate constants are identical, so the overall heteroFRET rate constant is the simple mean of the individual "a"- and "b"-chain donor rate constants, and the efficiencies E_i are thus expressed by equation S12, in which neither the infinite homoFRET rate constant nor, as also in Eq. 11 describing the case in which there is no donor-donor transfer, the common excitation-weighted average lifetime $\langle\tau_{0D}\rangle$ of the donors in absence of heteroFRET, appear:

$$E_i = \frac{1}{n}\sum_{i=1}^{n} \frac{\frac{1}{2}\left(\frac{3}{2}\kappa_{aai}^2\left(\frac{R_0}{R_{aai}}\right)^6 + \frac{3}{2}\kappa_{abi}^2\left(\frac{R_0}{R_{abi}}\right)^6 + \frac{3}{2}\kappa_{bbi}^2\left(\frac{R_0}{R_{bbi}}\right)^6 + \frac{3}{2}\kappa_{bai}^2\left(\frac{R_0}{R_{bai}}\right)^6\right)}{1 + \frac{1}{2}\left(\frac{3}{2}\kappa_{aai}^2\left(\frac{R_0}{R_{aai}}\right)^6 + \frac{3}{2}\kappa_{abi}^2\left(\frac{R_0}{R_{abi}}\right)^6 + \frac{3}{2}\kappa_{bbi}^2\left(\frac{R_0}{R_{bbi}}\right)^6 + \frac{3}{2}\kappa_{bai}^2\left(\frac{R_0}{R_{bai}}\right)^6\right)}$$

(Eq. S12)

which leads to an overall average donor-to-acceptors FRET efficiency for the bent configuration of about 11.3 %.

However, in assuming extremely rapid homoFRET, and thus being independent of the actual one-way rate constant, $k_{ddi} = \frac{1}{\langle\tau_{0D}\rangle}\frac{3}{2}\kappa_{ddi}^2\left(\frac{R_{0h}}{R_{ddi}}\right)^6$, for reversible donor-donor transfer for each individual conformer *i*, this expression usually, and certainly in the present case, represents a severe oversimplification. Instead, when the exchange transfer rate constant is not effectively infinite, equation S13 applies:

$$E_i = 1 - \frac{1}{2}[(1 + 2\beta_i)\langle\tau_{1i}\rangle + (1 - 2\beta_i)\langle\tau_{2i}\rangle] \qquad \text{(Eq. S13)}$$

where the excitation-weighted average lifetimes $\langle\tau_{1,2i}\rangle$, defined here as the average lifetimes of conformer *i* in the presence of acceptors **normalized to the effective common excitation-averaged lifetime in absence of acceptors, $\langle\tau_{0D}\rangle$,** are calculated using equations S14-S16, while β_i is given by equation S17:

$$\langle \gamma_{1,2i} \rangle = \frac{1}{\langle \tau_{1,2i} \rangle} = \left\{ \left[X_{ai} + X_{bi} + 2\frac{3}{2}\kappa_{ddi}^2 \left(\frac{R_{0h}}{R_{ddi}} \right)^6 \right] \mp \sqrt{(X_{ai} - X_{bi})^2 + 4\left[\frac{3}{2}\kappa_{ddi}^2 \left(\frac{R_{0h}}{R_{ddi}} \right)^6 \right]^2} \right\} \quad \text{(Eq. S14)}$$

where the appropriately equivalently normalized X_{ai} and X_{bi} are defined by:

$$X_{ai} = 1 + \frac{3}{2}\kappa_{aai}^2 \left(\frac{R_0}{R_{aai}} \right)^6 + \frac{3}{2}\kappa_{abi}^2 \left(\frac{R_0}{R_{abi}} \right)^6 \quad \text{(Eq. S15)}$$

$$X_{bi} = 1 + \frac{3}{2}\kappa_{bbi}^2 \left(\frac{R_0}{R_{bbi}} \right)^6 + \frac{3}{2}\kappa_{bai}^2 \left(\frac{R_0}{R_{bai}} \right)^6 \quad \text{(Eq. S16)}$$

and:

$$\beta_i = \frac{\frac{3}{2}\kappa_{ddi}^2 \left(\frac{R_{0h}}{R_{ddi}} \right)^6}{\sqrt{(X_{ai} - X_{bi})^2 + 4\left[\frac{3}{2}\kappa_{ddi}^2 \left(\frac{R_{0h}}{R_{ddi}} \right)^6 \right]^2}} \quad \text{(Eq. S17)}$$

Using a homoFRET Förster separation for GFP, R_{0h}, of 4.73 nm (the average of values given by Hink *et al*. (Ref. S3) for κ^2 = 1 and κ^2 = 4, each scaled to κ^2 = 2/3) and the previously used refractive index, the calculated overall FRET efficiency, $\langle E \rangle$, using this equation averaged over all the conformers for the bent IgEFc was 9.27%, with individual conformers having a wide spread of higher and lower efficiencies. This is very close to the value (9.17%) determined assuming the absence of inter-donor homoFRET, and thus still in very good agreement with the experimental results. If the experimental errors from the measurement of R_0 and R_{0h} were to be conservatively taken as ± 0.1 nm, then the calculated heteroFRET efficiencies of (9.2 ± 0.7)% and (9.3 ±0.8)% in the absence and presence of homoFRET, respectively, would be experimentally indistinguishable. In the case of the extended IgEFc-based models, inclusion of homoFRET in the calculations, even with complete sharing of excitation between the two donors, resulted in only a marginally increased efficiency (from 0.54% to 0.55%). When the actual rate constant for donor-donor transfer was taken into account, the expected heteroFRET efficiency was found to decrease slightly, to 0.50%.

The necessary simplification of the system kinetics required to make these calculations is mitigated by the fact that: (1) even though the kinetic behaviour of the donor excited states may be complex, they must be very similar spectroscopically (no obvious difference in their emission spectra), as must also be the case if there are two ground states; (2) the overall FRET efficiency is low (especially for the extended IgEFc model), so the impact of the photophysical kinetic complexities should also be small; (3) even if each individual donor is exchanging between two excited states, the simple monoexponential anisotropy decay (due to rotational depolarization) for the isolated eGFP (Fig. 3E in the main text) with a zero-point anisotropy near the limiting value (so essentially no ultrafast depolarization) indicates that there is no significant change in the transition moment vector orientation between the two excited state species, and presumably similarly so for the individual mRFP acceptors, so that there is no ambiguity with respect to the orientation factors for either the homoFRET or heteroFRET; (4) the calculated and experimental values are in good agreement. Taken together, these suggest that, although the current calculations were only possible through a simplification of the photophysical processes, this has not been critical. This contention is very much

strengthened by our use of the individual orientation factor value appropriate for each and every model, rather than arbitrarily using the 2/3 value incorporated into R_0 and R_{0h} (see below and **Additional Analysis** for a more detailed examination of the role of the orientation factor).

Modelling homoFRET depolarization kinetics for bent-form N-terminal (eGFP-IgEFc) and C-terminal (IgEFc-eGFP) constructs

Experimental determination of steady-state anisotropies of both separately doubly eGFP-labelled C-and N-terminal constructs (the latter having eGFP substituted for the mRFP acceptor at its sites in the heteroFRET system) showed by red-edge repolarization that a significant degree of homoFRET between the two eGFP labels occurs in both cases (Fig. 3*B* in the main text). This was confirmed by time-resolved depolarization measurements on these constructs (Fig. 3F in the main text). Here homoFRET is identified by a marked deviation from the monoexponential anisotropy decay expected for rotation alone (as a harmonic combination of local segmental and whole-body rotational relaxation) in the time-window set by the short excited-state lifetimes, such as observed for free eGFP (Fig. 3*E* in main text), and did not change in either case on addition of the soluble sFcεRIα fragment which binds to them (Figs. 3*C* and *D* in the main text). For a single conformation of the labelled protein, the overall time-dependent depolarization, including that due to homoFRET and that due to rotation, whose effects multiply each other, may be expressed using the same nomenclature as above, by equation S18 (cf. Eq. 9 and references thereto in the main text):

$$r_i(t) = \frac{r_0}{2}\left([(1 - d_{Tddi})] \exp\left[-2\frac{t}{\langle\tau_{0D}\rangle}\frac{3}{2}\kappa^2_{ddi}\left(\frac{R_{0h}}{R_{ddi}}\right)^6\right] + (1 + d_{Tddi}) \right) \exp\left[-\frac{t}{\langle\phi\rangle}\right] \qquad \text{(Eq. S18)}$$

where r_0 is the time-zero (zero-point) anisotropy, $\langle\phi\rangle$ the harmonically-combined average rotational correlation time, $\langle\tau_{0D}\rangle$ again the common excitation-averaged lifetime of the fluorophores, and d_{Tddi} the homoFRET depolarization factor (see Ref. 34 in the main text) given by equation S19:

$$d_{Tddi} = \frac{3}{2}\cos^2\theta_{Tddi} - \frac{1}{2} \qquad \text{(Eq. S19)}$$

in which θ_{Tddi} is the angle between the transition moment vectors of the fluorophores. In the present case of multiple conformers in stable equilibrium on time-scales long compared with the excited-state lifetime, the resulting average, multi-exponential anisotropy decay is given by equation S20:

$$\langle r(t)\rangle = \frac{r_0}{2}\left(\frac{1}{N}\sum_{i=1}^{N}[(1 - d_{Tddi})] \exp\left[-2\frac{t}{\langle\tau_{0D}\rangle}\frac{3}{2}\kappa^2_{ddi}\left(\frac{R_{0h}}{R_{ddi}}\right)^6\right] + (1 + d_{Tddi}) \right) \exp\left[-\frac{t}{\langle\phi\rangle}\right] \qquad \text{(Eq. S20)}$$

with constant r_0 and $\langle\phi\rangle$ taken, to a first approximation, to be common. This equation was fitted to the convoluted experimentally time-resolved depolarization of the constructs (see main text). In order to do this: (1) the homoFRET parameters for each conformer (separation R_{ddi}, relative orientation θ_{Tddi} and orientation factor κ^2_{ddi}) were fixed at the values obtained from the models; (2) the common excitation-weighted average lifetime $\langle\tau_{0D}\rangle$ values used were 2.71 ns and 2.68 ns for the eGFP-IgEFc (N-terminal) and IgEFc-eGFP (C-terminal) constructs, respectively, and were calculated from the parameters of the biexponential decay (see Eq. 3 in the main text) obtained by reconvolution least-

squares analysis of the total emission decay curve generated from the polarized components; (3) experimentally measured values for r_0 (to a resolution of 0.001) and $\langle\phi\rangle$ (to a resolution of 0.1 ns) were obtained from photon-counting weighted best-fits for impulse response anisotropy decays to the experimental anisotropy decays starting just prior to the peak of the excitation pulse. These optimized-fit responses were found to be in quite remarkably good correspondence with the data, as seen in Fig. 3F in the main text. The excellent goodness-of-fit in both cases is confirmed here by presentation of the weighted residuals for these fits (see Supplemental Fig. S8A). These were calculated using variances for the anisotropies propagated from the photon counts of the original polarized decay component data, taking into account G-factor normalization. A similar procedure was also used for the optimized fit of the simple monoexponential anisotropy decay of eGFP shown in Fig. 3*E* in the main text (weighted residuals shown in Supplemental Fig. S8A). The time-zero anisotropies, r_0, and average rotational correlation times, $\langle\phi\rangle$, recovered are shown in Supplemental Table S4.

The excellent correspondence of the model predictions for time-resolved homoFRET depolarization with the experimental data, despite the shortcomings of the assumptions invoked (see previous discussion, and also the **Additional Analysis** below, where two of these assumptions are examined in more detail), lends strong support to the veracity of using the modelling for calculation of not only the detailed course of homoFRET depolarization, but also the heteroFRET efficiency.

Additional Analysis

Analysis of separations and relative orientations of donors and acceptors in the bent and extended fusion protein models of eGFP(surrogate for mRFP)-IgEFc-eGFP

For both the bent and extended IgEFc configurations, the separations R_{jki} $([j,k]=[a,b])$ between the fluorophores at opposite (C-terminal and N-terminal) ends of the construct in the 1300 cases i, showed a distribution that was fairly symmetrical but not quite bell-shaped, with means ± standard deviations of about (8.5 ± 2.1) nm and (9.2 ± 2.3) nm within chains ("aa" and "bb"), respectively, and (11.7 ± 1.9) nm and (9.4 ± 2.1) nm for the cross-chain ("ab" and "ba") cases, respectively (illustrated indirectly in Supplemental Fig. S6). The corresponding parameters for the extended configuration were (14.9 ± 1.7) nm and (14.7 ± 1.8) nm, (13.6 ± 2.3) nm and (13.8 ± 2.3) nm, respectively. The similar standard deviations for both model sets indicate that, even though the conformations of IgEFc are very different between its bent and extended configurations, this has not affected the range of conformations that the attached FPs can adopt, these being displaced in concert towards each other in the bent configuration.

In both the bent and extended IgEFc models, the probability densities for the distributions of the heteroFRET orientation factors κ^2_{jki} were very close to a random distribution, indicated in Supplemental Fig. S6 and more definitively demonstrated overall in Supplemental Fig. S7. No bias towards any specific range of values was observed, with the means for the individual *jk* sets ranging from 0.6 to 0.675. Importantly, the dot plots of κ^2_{jki} against R_{jki} (Supplemental Fig. S6) revealed that this random distribution appeared to be essentially true for all separations. Again, the fact that random distributions occur for both the extended and bent configurations supports the expectation that the Cε2 domain pair moves as a unit, as does the Cε4 domain pair.

The C-terminal donor-donor separations R_{ddi} also exhibited a more-or-less bell-shaped distribution, with a separation of (6.4 ± 1.5) nm (illustrated indirectly in Supplemental Fig. S9A).

Since the Förster homoFRET separation R_{0h} for eGFP is 4.73 nm, large effects of inter-donor homoFRET on the overall heteroFRET efficiency of individual conformers exhibiting the lower range of separations may be expected. However, as indicated above, upon averaging across all 1300 modeled conformers, for which again the orientation factors were close to randomly distributed (see below), the individual increases and decreases in eventual heteroFRET efficiency almost completely cancel each other out. As a consequence, the overall heteroFRET efficiency differs insignificantly from the scenario without donor-donor excited-state exchange.

The calculated rate and extent of depolarization due to homoFRET between the two C-terminal eGFPs differs enormously across the individual model conformations as shown by the selection of individual anisotropy decays displayed in Supplemental Fig. S11. The rate variation over and above that due to the separational distribution again arises from the near-random distribution of orientation factors (and is also essentially independent of separation) with a κ^2 value averaged across the conformers of 0.65. The striking variation in the extent of depolarization resides in the extent of the randomness of the angle between the two transition moment vectors, **D** and **A**. In turn, this produces a close to random distribution of the depolarization factors d_T as shown in Supplemental Fig. S9A and S10; this randomness was also essentially independent of separation. With the exception of the limitation of the dependence of the upper value of the orientation factor on the angle θ_T between the vectors **D** and **A**, and thus on the depolarization factor (Ref. S11), the distributions of the orientation and depolarization factors do appear to be correlated to some extent (see Supplemental Fig. S9B), even though separately they have close to random distributions. Nevertheless, the very disparate individual rates and extents of homoFRET depolarization (Supplemental Fig. S11) lead to an average homoFRET depolarization that is in excellent agreement with the experimental anisotropy decays (see Fig. 3*F* in the main text and Supplemental Fig. 8A). For the eGFP-IgEFc models, the distribution of the inter-donor separations was less symmetrical than that for the IgEFc-eGFP models, instead being somewhat biased towards greater separations. Given that the mean separation in this case was (8.0 ± 1.8) nm, taken together with the random distributions of the orientation and depolarization factors independent of the separation, less homoFRET depolarization would be expected, and this is indeed observed experimentally. Furthermore the calculation of the homoFRET depolarizations predicted from the models in this case is again found to be in very good agreement with the experimental findings as shown in Fig. 3*F* in the main text and Supplemental Fig. S8A.

Effects of applying a more exact form of the orientation factor in the model calculations for both heteroFRET and homoFRET

A more exact form of the orientation factor κ^2 is a dynamic average, $\langle\kappa^2\rangle_d$:

$$\langle\kappa^2\rangle_d = \kappa^{x2}\langle d_T^x\rangle^2 + \frac{2}{3}(1 - \langle d_T^x\rangle) + (\cos^2\theta_{DR} + \cos^2\theta_{AR})\langle d_T^x\rangle(1 - \langle d_T^x\rangle)$$

where the dynamic depolarization factor $\langle d_T^x\rangle$ is estimated as $\sqrt{r_0/0.4}$, and taken to be held in common by donor and acceptor in the present case of GFP-type fluorophores, while $\kappa^{x2} = (\cos\theta_{DA} - 3\cos\theta_{DR}\cos\theta_{AR})^2$ corresponds with the orientation factor for the mean transition moment orientations, to which $\langle\kappa^2\rangle_d$ is reduced when there is no dynamic depolarization (see Refs. 44 and 50 in the main text). The main effect of this consideration for the close to statically randomly oriented donor-acceptor pairs in the present population of IgEFc conformers is to substantially reduce the occurrence of orientation factors near zero. While this hardly affects the population average of the orientation factor at all, it does result in very slightly increased overall average heteroFRET transfer

efficiencies: the values of 9.17%, 9.27%, and 11.26% calculated for cases without, with, and with ultra-rapid, donor-donor homoFRET, respectively, become 9.34%, 9.44%, and 11.39%, the first two remaining in excellent agreement with the experimental measurements.

On the other hand, this factor features strongly in the time-dependent fluorescence depolarization calculated for homoFRET between donor C-terminal eGFP moieties in the absence of acceptor FPs, and also – though to a somewhat lesser extent – in the N-terminal eGFP construct.

The overall anisotropy decays that it was calculated would be observed in the absence of rotational depolarization, taking into account the dynamic average orientation factors of the populations, were substantially faster than when it was not considered. However, these anisotropy decays could be matched over the accessible range of six average lifetimes of fluorescence decay (ca. 15 ns), to an equivalence well below the noise level of the experimental data, by trial assignment of rotational depolarization components of substantially lengthened rotational correlation times to the more accurate calculations for the two cases (*q.v.* below).

Effects of applying a different form of lifetime average in the model calculations for homoFRET.

Excitation-averaged lifetimes may also be defined as the reciprocals of excitation-averaged fluorescence decay rates, i.e., of reciprocal lifetimes, $1/\sum_i(\alpha_i/\tau_i)$, instead of directly averaged lifetimes (see Eq. 3 in the main text). This redefinition could also potentially have an appreciable effect on the the homoFRET-induced anisotropy decay calculated from the models, even though, in the present cases, these reciprocal forms are only about 0.1 ns smaller than the direct averages. However, since the eGFP donors exhibit intrinsic complex excited-state dynamics, it is not at all clear that the use of **any** single common average donor excited-state lifetime over an ensemble with such widely differing FRET efficiencies as are found in the present study (due to the broad distribution of separations and the essentially uncorrelated near random distribution of orientation factors) can be justified. On the other hand, the lack of information on the parameters of the complex excited-state dynamics of these fluorophores precludes any other approach.

In fact – rather more surprisingly than not – this potentially gross approximation appears to be sufficient. The differences ensuing from the use of either of the two averages are considerably smaller than the effect of considering the more accurate form of the orientation factor (above), though they act in the same direction. Taken together, the use of both excitation-averaged lifetimes and the more accurate orientation factors resulted in a lengthening of the fitted rotational correlation times. These changed from 54.5 ns and 38.6 ns (see Table S4) for calculated C-terminal IgEFc-eGFP and N-terminal eGFP-IgEFc homoFRET-induced anisotropy decays respectively, to 63.0 ns and 40.3 ns. The latter values more correctly define the apparent correlation times reported by these probes, which reflect both segmental and whole-molecule rotation in a way that depends on their orientations with respect to the axis of segmental rotation in each case.

The effect of using excitation-averaged lifetimes on homoFRET-induced anisotropy decay contrasts strongly with the calculation of heteroFRET efficiency estimates, even when homoFRET is also involved in that process, since there it is only the dimensionless **ratios** of fluorescence decay rates to FRET rates, both hetero- and homo-, that determine the efficiency outcome (compare Eqs. S1, S2, and Eqs. S13-S17).

SUPPLEMENTAL REFERENCES

(S1) Peter, M., Ameer-Beg, S. M., Hughes, M. K., Keppler, M. D., Prag, S., Marsh, M., Vojnovic, B., and Ng, T. (2005) Multiphoton-FLIM Quantification of the EGFP-mRFP1 FRET Pair for Localization of Membrane Receptor-Kinase Interactions. *Biophys. J.* **88,** 1224-1237

(S2) Release on refractive index of ordinary water substance as a function of wavelength, Temperature and pressure, September 1997, *International Association for the Properties of Water and Steam (IAPWS)*

(S3) Hink, M A., Visser, N. V., Borst, J. W., van Hoek, A., and Visser, A. J. W. G. (2003) Practical use of corrected fluorescence excitation and emission spectra of fluorescent proteins in Förster resonance energy transfer (FRET) studies. *J. Fluorescence* **13**, 186-188

(S4) Meech, S. R. (2009) Excited state reactions in fluorescent proteins. *Chem. Soc. Rev*. **38,** 2922-2934

(S5) Birks, J. B. (1970) *Photophysics of Aromatic Molecules*, Wiley, New York

(S6) Porter, G. B. (1972) Reversible energy transfer. *Theoret. Chim. Acta*, 24-265

(S7) Woolley, P., Steinhäuser, K. G., and Epe, B. (1987) Förster-type energy transfer – simultaneous 'forward' and 'reverse' transfer between unlike fluorophores. *Biophys. Chem*. ***26,*** 367-374

(S8) Laws, W. R., and Brand, L. (1979) Analysis of two-state excited-state reactions. The fluorescence decay of 2-naphthol. *J. Phys. Chem.* **83**, 795-802

(S9) Kowalczyk, A. A., Večeř, J., Hodgson, B. W., Keene, J. P., and Dale, R. E. (1996) Time-resolved fluorescence in micellar systems. A critical application to the partitioning of naphthalene in aqueous sodium dodecyl sulphate. *Langmuir* 12, 4358-4371

(S10) Szabo, A. (1984) Theory of fluorescence depolarization in macromolecules and membranes. *J. Chem. Phys.* **81**, 150-167

(S11) Dale, R.E., and Eisinger, J. (1975) *Polarized Excitation Energy Transfer* in *Biochemical Fluorescence: Concepts,* eds. Chen, R.F., and Edelhoch, H., Marcel Dekker, New York

Supplemental Data Tables

Table S1: Kinetic characterization of sFcεRIα binding to GFP/RFP labeled IgEFc and to a whole anti-4-hydroxy-3-nitrophenylacetyl specific monoclonal IgE (NP-IgE) using surface plasmon resonance (SPR). Both the k_a (the bimolecular association rate constant) and k_d (the dissociation rate constant) were obtained by global fit of the concentration dependence of observed sensorgrams to a 1:1 binding model using the manufacturer's (Biacore) software supplied with the instrument. [a] The equilibrium association constant (K_a) was derived from the kinetic rate constants in the following manner $K_a = k_a/k_d$. The values for k_a, k_d, and K_a are consistent with values obtained previously for sFcεRIα binding to IgE (see ref. 21).

	eGFP-IgEFc	**mRFP-IgEFc-eGFP**	**IgEFc-eGFP**	**mRFP-IgEFc**	**NP-IgE**
k_a **($M^{-1}s^{-1}$)**	$(4.24 \pm 0.02) \times 10^5$	$(4.95 \pm 0.02) \times 10^5$	$(4.97 \pm 0.02) \times 10^5$	$(4.79 \pm 0.02) \times 10^5$	$(2.67 \pm 0.01) \times 10^5$
k_d **(s^{-1})**	$(0.91 \pm 0.05) \times 10^{-5}$	$(1.19 \pm 0.04) \times 10^{-5}$	$(0.57 \pm 0.03) \times 10^{-5}$	$(1.56 \pm 0.03) \times 10^{-5}$	$(0.60 \pm 0.26) \times 10^{-5}$
K_a **(M^{-1})** [a]	4.7×10^{10}	4.2×10^{10}	8.7×10^{10}	3.1×10^{10}	4.5×10^{10}
χ^2	0.117	0.146	0.158	0.120	0.895

Table S2: Dual polarization interferometry (DPI) analysis of the mRFP-IgEFc-eGFP biosensor binding to the FcεRIα (expressed as a FcεRIα–IgG$_4$Fc fusion protein) compared to a whole anti-4-hydroxy-3-nitrophenylacetyl specific monoclonal IgE (NP-IgE) as well as the subfragments IgEFc and IgEFc$_{3-4}$. The data collected shows that the dimensions of the complex for whole IgE and the biosensor are similar, and that the IgEFc acts to project the Fabs (or N-terminal fluorescent domains) of IgE away from the binding surface. This is consistent with the models presented in figure 4.

Layer	Referenced to	Thickness (nm)	RI	Density (mgcm^{-3})	Mass (pgmm^{-2})	Stoichiometry
s-GMBS	Thiol Surface	1.297	1.51948	1012.4	1313.1	
FcεRIα–IgG$_4$Fc	s-GMBS	13.546	1.38599	278.9	3778.2	1.000
FcεRIα–IgG$_4$Fc + Block+ P20	s-GMBS	14.089	1.38511	274.1	3861.5	
IgEFc$_{3-4}$	FcεRIα–IgG$_4$Fc pre sample	0.385	1.41862	458.2	176.5	0.127
IgEFc	FcεRIα–IgG$_4$Fc pre sample	0.771	1.40448	380.6	293.4	0.140
NP-IgE	FcεRIα–IgG$_4$Fc pre sample	2.890	1.38242	259.3	749.0	0.136
mRFP-IgEFc-eGFP	FcεRIα–IgG$_4$Fc pre sample	2.690	1.37959	243.8	655.7	0.125

Table S3: Fluorescence lifetime fit parameters derived from time-resolved measurements on an mRFP-IgEFc-eGFP biosensor and controls, in the presence and absence of IgE ligands. The true average lifetime, $\bar{\tau}$, was calculated using Eq. 2 in the main text, and the excitation-weighted average lifetime, $\langle\tau\rangle$, was calculated using Eq. 3 in the main text. The true average lifetimes, $\bar{\tau}$, are shown graphically in Fig. 2*C* within the main text. The lifetime FRET efficiency, E_τ, was calculated from $\langle\tau\rangle$ using Eq. 4 in the main text and expressed as a percentage. All data is shown to 2 d.p. The lifetimes quoted are the averages of the lifetimes obtained in each of the n experiments ± standard deviations. N/A, not applicable. Errors associated with the E_τ values are the maximum errors in the calculation of the value based on the experimental standard errors of the $\langle\tau\rangle$ measurements. We note that both the true average and excitation-averaged lifetimes quoted ($\bar{\tau}$ and $\langle\tau\rangle$, respectively), as well as the efficiencies E_τ, were calculated from the α and τ values obtained from the relevant decay curve analyses which were not rounded down to 2 d.p., resulting in small discrepancies in the second d.p. of some of these averages as compared with those which may be calculated from the α and τ values presented.

	FRET Biosensor				**Controls**					
Parameter	**mRFP-IgEFc-eGFP (n = 5)**	**mRFP-IgEFc-eGFP + sFcεRIα (n = 5)**	**mRFP-IgEFc-eGFP + omalizumab Fab (n = 5)**	**mRFP-IgEFc-eGFP +der CD23 (n = 5)**	**IgEFc-eGFP + mRFP-IgEFc (n = 5)**	**IgEFc-eGFP + mRFP-IgEFc +sFcεRIα (n = 5)**	**IgEFc-eGFP + mRFP-IgEFc + omalizumab Fab (n = 5)**	**IgEFc-eGFP + mRFP-IgEFc +derCD23 (n = 5)**	**IgEFc-eGFP (n = 5)**	**eGFP (n = 12)**
τ_1 **(ns)**	2.71 ± 0.02	2.67 ± 0.02	2.76 ± 0.02	2.70 ± 0.01	2.84 ± 0.02	2.86 ± 0.01	2.88 ± 0.02	2.89 ± 0.03	2.85 ± 0.01	2.89 ± 0.04
α_1	0.82 ± 0.02	0.80 ± 0.01	0.84 ± 0.03	0.83 ± 0.01	0.89 ± 0.02	0.87 ± 0.01	0.83 ± 0.02	0.83 ± 0.04	0.89 ± 0.01	0.83 ± 0.04
τ_2 **(ns)**	1.24 ± 0.11	1.23 ± 0.06	1.40 ± 0.16	1.25 ± 0.05	1.27 ± 0.14	1.55 ± 0.06	1.70 ± 0.11	1.70 ± 0.18	1.27 ± 0.10	1.53 ± 0.22
α_2	0.18 ± 0.02	0.20 ± 0.01	0.16 ± 0.03	0.17 ± 0.01	0.11 ± 0.02	0.13 ± 0.01	0.17 ± 0.02	0.17 ± 0.04	0.11 ± 0.01	0.17 ± 0.04
$\bar{\tau}$ **(ns)**	2.57 ± 0.01	2.52 ± 0.01	2.64 ± 0.01	2.57 ± 0.01	2.76 ± 0.01	2.76 ± 0.01	2.76 ± 0.01	2.77 ± 0.01	2.76 ± 0.01	2.76 ± 0.01
$\langle\tau\rangle$ **(ns)**	2.45 ± 0.01	2.38 ± 0.01	2.54 ± 0.01	2.45 ± 0.01	2.69 ± 0.01	2.69 ± 0.01	2.69 ± 0.01	2.70 ± 0.01	2.67 ± 0.01	2.66 ± 0.01
E_τ **(%)**	8.9 ± 0.7	11.5 ± 0.7	5.6 ± 0.7	9.2 ± 0.8	N/A	N/A	N/A	N/A	N/A	N/A

Table S4: Fluorescence depolarization parameters calculated from the anisotropy decays for eGFP, free and fused N-terminally (eGFP-IgEFc) and C-terminally (IgEFc-eGFP) to the IgEFc. The zero-point anisotropy, r_0, and apparent average rotational correlation time, $\langle\phi\rangle$, were obtained by least-squares optimized fitting of the theoretical curves to the experimental anisotropy decay data as described in the Supplemental Methods. The fits to the data are shown in Figs. 3*E* and 3*F* in the main text with residuals shown in Supplemental Fig. S8A. The approximate standard deviations for the rotational correlation times are equated with the approximate 67% confidence limits, obtained as values of $\langle\phi\rangle$ greater and smaller than the best-fit value, and were found by plotting total chi-squared values for the fits against $\langle\phi\rangle$, corresponding to one reduced chi-squared ($\chi_v^2 = \frac{1}{N-1}\sum_{i=1}^{N}\chi_i^2$) above the minimum total chi-squared value $\sum_{i=1}^{N}\chi_i^2$.

Protein	r_0	$\langle\phi\rangle$ (ns)	χ_v^2
eGFP	0.388	19.8 ± 0.2	0.9192
eGFP-IgEFc	0.378	38.6 ± 0.3	1.0195
IgEFc-eGFP	0.374	54.5 ± 0.7	1.0303

SUPPLEMENTAL FIGURE LEGENDS

FIGURE S1: **Amino acid sequences of all fluorescent protein constructs**. See key for color coding, additional residues refer to non-native additions to the protein sequences to link domains.

FIGURE S2: **Size exclusion gel filtration profiles of fluorescent IgE fusion proteins.** Samples were run at 0.75 ml/min in 50mM Tris 150mM NaCl (TBS) (pH 7.2) on a Superdex 200 10/300 column (GE Biosciences); protein was detected by UV absorbance at 280 nm. The earlier elution of the mRFP-IgEFc-eGFP is consistent with its greater molecular weight. The overlaid traces were aligned to their injection points, and the absorbances normalized to show a peak absorbance of 1.

FIGURE S3: **Gel filtration profiles of fluorescent IgE fusion proteins with and without sFcεRIα.** Samples were run at 0.75 ml/min in TBS (pH 7.2) on a Superdex 200 10/300 column (GE Biosciences); protein was detected by fluorescence of the eGFP/mRFPs at 510nm (excitation 488nm) (left hand panels) and UV absorbance at 280nm (right hand panels). Movement of the gel filtration elution profile, indicated by the arrow over the top of the peaks in A and C, shows complete saturation of binding by all the IgE constructs with sFcεRIα. Top two panels (A and B) show the control molecules, bottom two panels (C and D) the biosensor. In each case the overlaid traces were aligned to their injection points. In the case of the control experiments (A and B) only one peak is apparently seen for the mixture of mRFP-IgEFc and IgEFc-eGFP mixtures due to their very similar size (see Figure S2).

FIGURE S4: **eGFP shows a biexponential fluorescence decay.** Decay data (excitation 468nm, emission 510nm, emission monochromator bandwidth 4nm) were collected using an Edinburgh Instruments Lifespec employing time-correlated single-photon counting (TCSPC) and fitted to either a biexponential or monoexponential decay model using TRI2 (see Ref. 28, main text). The line on the uppermost plot indicates the fit line for a biexponential model (fit parameters are shown in table S3), with the photon-counting weighted residuals (in units of standard deviations from the fit) shown in the middle panel. The residuals for a mono-exponential fit are shown in the bottom panel.

FIGURE S5: **Fluorescence decay control experiments.** A. Fluorescence decays and biexponential fits (line plots), and their photon-counting weighted residuals, for the control proteins – IgEFc-eGFP alone (open black circles), or mRFP-IgEFc and IgEFc-eGFP (open red circles). Green circles are the instrument response function (IRF). Complete overlap of the fits indicates there to be no discernable inter-molecular FRET. B. Fluorescence decays and biexponential fits (line plots), and their photon-counting weighted residuals, for control molecules mRFP-IgEFc and IgEFc-eGFP with (open red circles) and without (open black circles) sFcεRIα. Green circles are the instrument response function (IRF). Complete overlap of the fits indicates that there is no discernible FRET on binding of the control molecules to sFcεRIα.

FIGURE S6: **Close-to-random population distributions of the orientation factor (κ^2) for heteroFRET in the bent configuration mRFP-IgEFc-eGFP biosensor**. For each of the 1300 bent configuration biosensor models, the orientation factors (κ^2) and separations (R) between the fluorophores were determined for the different combinations of donor (eGFP located on the C-terminus of each chain –"a" and "b" of the IgEFc dimer) and acceptor (eGFP used as a structural surrogate for mRFP located on the N-terminus of each chain – "a" and "b" of the IgEFc dimer) combinations. A and C show the distributions for the "a"-chain donor to "a"-chain acceptor (CaNa,

red circles) and "a"-chain donor to "b"-chain acceptor (CaNb, red circles) heteroFRET pairs. B and D show the distributions for the "b"-chain donor to "b"-chain acceptor (CbNb, pink circles) and "b"-chain donor to "a"-chain acceptor (CbNa, red circles) heteroFRET pairs. In all cases the κ^2 distributions are very close to that for truly random orientations (see also Supplemental Fig. S7) and are also approximately independent of donor-acceptor separation *R*. C and D show semi-log plot versions of the data in A and B to emphasize the preponderance of small κ^2 values in the distributions. It should be noted that the vertically summed density of points also indicates roughly the shape and extent of the distributions of *R*-values. Similar orientation factor distributions are found for the extended configuration, together with greater, but similarly distributed, donor-acceptor separations.

FIGURE S7: **The overall distribution of the orientation factor (κ^2) for heteroFRET for the four donor-acceptor pairs (CaNa, CaNb, CbNb, CbNa) shown in Supplemental Fig. S6 is close to random.** A**,** Histogram (light blue columns) of the frequency distribution of κ^2 (the probability density, $p(\kappa^2)$) for κ^2 values calculated from the coordinates of the N = 1300 models for each donor-acceptor pair, binned at intervals of 0.1, to compare with the similarly binned $p(\kappa^2)$ for perfectly random orientations (dark blue dots). The average heteroFRET orientation factor for the models, $\langle\kappa^2\rangle$ = 0.631 ± 0.040, is close to the 2/3 values for random orientations. The red error bars, shown only every other band for clarity, represent the symmetric ± standard deviations about the truly random values (dark blue dots), which were calculated as the difference between the probability distributions $P(\kappa^2) = \int_0^{\kappa^2} p\,(\kappa^2)d\kappa^2$ for truly random orientations at the upper and lower extremes of the band (see, for example, Refs. 44 and 50 in the main text):

$$P(\kappa^2) = \begin{cases} \ln\left(2+\sqrt{3}\right)\sqrt{\dfrac{\kappa^2}{3}} & 0 < \kappa^2 \le 1 \\ \sqrt{\dfrac{\kappa^2}{3}}\left[\ln\left(2+\sqrt{3}\right) - \ln\left(\sqrt{\kappa^2-1}+\sqrt{\kappa^2}\right)\right] + \sqrt{\dfrac{\kappa^2-1}{3}} & 1 \le \kappa^2 \le 4 \end{cases}$$

These standard deviations are those expected for a perfectly random distribution given a total of 4N κ^2 values in the histogram: $\sigma[p(\kappa^2)] = \sqrt{p(\kappa^2)/4N}$. B. A semi-log scaled histogram with the same contents as in A. This clarifies the small probability densities for large values of κ^2. The absence of any models in the two highest bands arises due to the maximum value for κ^2 derived from the models being ~3.78. The absence of the error bar for the last band is due to the negative lower end (the estimated standard deviation is larger than the value itself). Again, a similarly close-to-random distribution is observed for the extended configuration (data not shown).

FIGURE S8: **Anisotropy decay experiments provide additional validation that homoFRET occurs between the two eGFP molecules on the eGFP-IgEFc and IgEFc-eGFP constructs.** A. Photon-counting weighted residuals propagated from the polarized decays taking into account the G-factor (the difference between the data and the fit at each point in units of expected standard deviations) for the fits of the theoretically calculated anisotropy decays to the measured anisotropy decays for eGFP (green circles), eGFP-IgEFc (blue circles), and IgEFc-eGFP (red circles) shown in Fig. 3E and F in the main text. B. Anisotropy decays of eGFP-IgEFc with (open blue circles) and without (filled blue circles) bound sFcεRIα. The instrument response function (IRF) is shown in black. C. Anisotropy decays of IgEFc-eGFP with (open red circles) and without (filled red circles)

bound sFcεRIα. Binding to sFcεRIα had no effect on the anisotropy decay of either N-terminally, or C-terminally attached eGFP constructs.

FIGURE S9: **Analysis of the distributions of the homoFRET depolarization factors (d_T) and inter-fluorophore separations (R), and of the relationship between d_T and the homoFRET orientation factors (κ^2).** The results presented here are for the bent configuration of the C-terminal homoFRET pair, but similar conclusions can be drawn for the extended configuration, and for both bent and extended configurations of the N-terminal pair (data not shown). A. For each of the 1300 bent-form models the depolarization factor, $d_T = (3/2)\cos^2\theta_T - (1/2)$, where θ_T is the angle between the transition moments of the two fluorophores, and the separation between the C-terminal donor fluorophores on the "a"- and "b"-chains (R_{CaCb}) were calculated. The scatter plot illustrates that the distribution of d_T and is approximately independent of R_{CaCb}. B. For each of the 1300 models the homoFRET orientation factor, κ^2, was calculated from $\kappa^2 = (\cos\theta_T - 3\cos\theta_a\cos\theta_b)^2$, where θ_a and θ_b are the angles between the transition moments for the fluorophores on the "a"- and "b"- chains, respectively, and the vector separating them. The relationship between these and the calculated depolarization factor is also displayed in a scatter plot. For comparison, the yellow background covers the possible available range of κ^2 values; this spans the range from the minimum value of zero to the maximum possible value given by the expression $\kappa^2_{max} = 9/4 \le (1/4)\left[3 + \sqrt{(1+2d_T)/3}\right]^2 \le 4$ (see Supplemental Ref S11). Within these limits a wide range of κ^2 values was found for all d_T values even when the two fluorophores are either perpendicular or close to perpendicular to each other. We note that there is a preponderance of zero or close-to-zero κ^2 values over the whole range of depolarizations. Despite the fact that the banded probability density for d_T , shown in Supplemental Fig. S10, indicates that the distribution of θ_T is also very close to random, the κ^2 versus d_T scatter plot also reveals that there is some degree of correlation between them. For example, although both parameters, when separately considered, indicate close-to-random angular distributions (see also the average values presented below), there appears to be some selection of angles θ_a, θ_b and θ_T, such that pairings of higher values of κ^2 and d_T (roughly for the top right quadrant defined by $[3/2 \le \kappa^2 \le \kappa^2_{max}, 0 \le d_T \le 1]$ are rarer than in a completely random population (not shown). For the C-terminal construct (IgEFc-eGFP), the average values of the orientation and depolarization factors are: $\langle\kappa^2\rangle$ = 0.649 ± 0.038 (close to the value of 2/3 for randomly orientated fluorophores); and $\langle d_T\rangle$ = 0.0252 ± 0.0023 (close to the random average of zero). The equivalent average values for the N-terminal construct (eGFP-IgEFc) are: $\langle\kappa^2\rangle$ = 0.595 ± 0.037; and $\langle d_T\rangle$ = 0.0055 ± 0.0014, which are again close to the random average values.

FIGURE S10: **The distribution of the homoFRET depolarizarion factor, d_T, for the two eGFPs on the "a"- and "b"-chains of the IgEFc-eGFP construct shown in Supplemental Fig. S9 is close-to-random.** B. A histogram (filled blue bars) of the frequency distribution (the probability density, $p(d_T)$), binned at 0.1 intervals for the d_T values calculated from the coordinates of the N = 1300 models. Averaging over all models gives a value $\langle d_T\rangle$ = 0.0252 ± 0.0023. The red error bars, shown only every other band for clarity, represent the ± standard deviation about the $p(d_T)$ calculated from the models. The dark blue dots represent the banded values of $p(d_T)$ for truly random transition moment orientations and were obtained as the difference between the values of the probability distribution $P(d_T)$ at the upper and lower extremes of the band as given by the expression $P(d_T) = \int_0^{d_T} p(d_T)\, d(d_T) = \sqrt{\frac{1}{3}(1+2d_T)}$. This illustrates the close correspondence between the probability distributions for the values of d_T calculated from the models and that expected for a distribution of

perfectly randomly oriented donor and acceptor transition moments. B. A semi-log scaled histogram with the same contents as in *A*. This clarifies the small probability densities of the models in which there are higher values of d_T. A similar distribution was also found for the N-terminal construct (eGFP-IgEFc; data not shown) yielding an average depolarization factor $\langle d_T \rangle$ = 0.0055 ± 0.0014.

FIGURE S11: **Individual IgEFc-eGFP conformers selected from the 1300 models show a large range of effects on the anisotropy decay due to widely differing rates and extents of depolarization due to homoFRET superimposed on and segmental rotational depolarization.** The anisotropy decays are plotted on a semi-logarithmic scale to allow direct comparison with the experimental results in Fig. 3*E* and *F*, with the average across all 1300 models previously shown in Fig 3*F* reproduced here as the black curve. For the representative models, as well as the average over all 1300 models, decays are shown in two formats. In each case the colored solid lines, which curve to greater or lesser extents, show the overall anisotropy decays. To illustrate the differing impacts of homoFRET depolarization in each of the model conformers, the part of the anisotropy decays due solely to rotational depolarization (with average rotational correlation time, $\langle \phi \rangle$ = 54.5 ns) is represented (since the plot is semi-logarithmic) by color-coordinated linear dotted lines whose zero-time intercepts are governed by $r_0\,(1 + d_T)/2$, where d_T is the reorientational depolarization factor introduced by reversible homoFRET between the fluorophores. Hence, it can be seen (to a first approximation) that the curvature of the lines is directly related to the rate of homoFRET that occurs in each model based on the different separations and orientation factors for the two eGFP groups, whereas the extent of the curved region depends only on the angle θ_T between the two transition moments. The solid blue curve shows a case where there is an at least close to zero rate constant for homoFRET (but a very large potential homoFRET depolarization is evidenced by the corresponding dark blue dotted line), whereas the dark green curve shows a case where very rapid homoFRET occurs, coupled to a large homoFRET depolarization. The other curves (red, light green, cyan, and pink) show intermediate cases between these two extremes. Here again, the roles played by the rate and by the extent of homoFRET depolarization, can be seen by comparing, in particular, the red and light green curves. For the model conformer shown in the red curve, very slow homoFRET occurs over a fairly large depolarization range (about 0.07, corresponding to an angle θ_T of about 30°), while for the model conformer shown in the light green curve there is much faster homoFRET depolarization, essentially complete within 2 ns but occurring over only a very small depolarization range. Similar cases to those shown here are observed for the eGFP-IgEFc models, but with more rapid segmental rotation ($\langle \phi \rangle$ = 38.6 ns).

Supplemental Figure S1:

Signal peptide; eGFP; IgEFc; mRFP; additional residues

eGFP-IgEFc

MSVPTQVLGLLLLWLTDARCDIMVSKGEELFTGVVPILVELDGDVNGHKFSVSGEGEGDATYGKLTLKF
ICTTGKLPVPWPTLVTTLTYGVQCFSRYPDHMKQHDFFKSAMPEGYVQERTIFFKDDGNYKTRAEVKFE
GDTLVNRIELKGIDFKEDGNILGHKLEYNYNSHNVYIMADKQKNGIKVNFKIRHNIEDGSVQLADHYQQ
NTPIGDGPVLLPDNHYLSTQSALSKDPNEKRDHMVLLEFVTAAGDIVASRDFTPPTVKILQSSCDGGGH
FPPTIQLLCLVSGYTPGTIQITWLEDGQVMDVDLSTASTTQEGELASTQSELTLSQKHWLSDRTYTCQV
TYQGHTFEDSTKKCADSNPRGVSAYLSRPSPFDLFIRKSPTITCLVVDLAPSKGTVQLTWSRASGKPVN
HSTRKEEKQRNGTLTVTSTLPVGTRDWIEGETYQCRVTHPHLPRALMRSTTKTSGPRAAPEVYAFATPE
WPGSRDKRTLACLIQNFMPEDISVQWLHNEVQLPDARHSTTQPRKTKGSGFFVFSRLEVTRAEWEQKDE
FICRAVHEAASPSQTVQRAVSVNPGK*

mRFP-IgEFc-eGFP

MSVPTQVLGLLLLWLTDARCDIMASSEDVIKEFMRFKVRMEGSVNGHEFEIEGEGEGRPYEGTQTAKLK
VTKGGPLPFAWDILSPQFQYGSKAYVKHPADIPDYLKLSFPEGFKWERVMNFEDGGVVTVTQDSSLQDG
EFIYKVKLRGTNFPSDGPVMQKKTMGWEASTERMYPEDGALKGEIKMRLKLKDGGHYDAEVKTTYMAKK
PVQLPGAYKTDIKLDITSHNEDYTIVEQYERAEGRHSTGAPVASRDFTPPTVKILQSSCDGGGHFPPTI
QLLCLVSGYTPGTIQITWLEDGQVMDVDLSTASTTQEGELASTQSELTLSQKHWLSDRTYTCQVTYQGH
TFEDSTKKCADSNPRGVSAYLSRPSPFDLFIRKSPTITCLVVDLAPSKGTVQLTWSRASGKPVNHSTRK
EEKQRNGTLTVTSTLPVGTRDWIEGETYQCRVTHPHLPRALMRSTTKTSGPRAAPEVYAFATPEWPGSR
DKRTLACLIQNFMPEDISVQWLHNEVQLPDARHSTTQPRKTKGSGFFVFSRLEVTRAEWEQKDEFICRA
VHEAASPSQTVQRAVSVNPGKPVATMVSKGEELFTGVVPILVELDGDVNGHKFSVSGEGEGDATYGKLT
LKFICTTGKLPVPWPTLVTTLTYGVQCFSRYPDHMKQHDFFKSAMPEGYVQERTIFFKDDGNYKTRAEV
KFEGDTLVNRIELKGIDFKEDGNILGHKLEYNYNSHNVYIMADKQKNGIKVNFKIRHNIEDGSVQLADH
YQQNTPIGDGPVLLPDNHYLSTQSALSKDPNEKRDHMVLLEFVTAAGI

mRFP-IgEFc

MSVPTQVLGLLLLWLTDARCDIMASSEDVIKEFMRFKVRMEGSVNGHEFEIEGEGEGRPYEGTQTAKLK
VTKGGPLPFAWDILSPQFQYGSKAYVKHPADIPDYLKLSFPEGFKWERVMNFEDGGVVTVTQDSSLQDG
EFIYKVKLRGTNFPSDGPVMQKKTMGWEASTERMYPEDGALKGEIKMRLKLKDGGHYDAEVKTTYMAKK
PVQLPGAYKTDIKLDITSHNEDYTIVEQYERAEGRHSTGAPVASRDFTPPTVKILQSSCDGGGHFPPTI
QLLCLVSGYTPGTIQITWLEDGQVMDVDLSTASTTQEGELASTQSELTLSQKHWLSDRTYTCQVTYQGH
TFEDSTKKCADSNPRGVSAYLSRPSPFDLFIRKSPTITCLVVDLAPSKGTVQLTWSRASGKPVNHSTRK
EEKQRNGTLTVTSTLPVGTRDWIEGETYQCRVTHPHLPRALMRSTTKTSGPRAAPEVYAFATPEWPGSR
DKRTLACLIQNFMPEDISVQWLHNEVQLPDARHSTTQPRKTKGSGFFVFSRLEVTRAEWEQKDEFICRA
VHEAASPSQTVQRAVSVNPGK

IgEFc-eGFP

MSVPTQVLGLLLLWLTDARCDPVASRDFTPPTVKILQSSCDGGGHFPPTIQLLCLVSGYTPGTIQITWL
EDGQVMDVDLSTASTTQEGELASTQSELTLSQKHWLSDRTYTCQVTYQGHTFEDSTKKCADSNPRGVSA
YLSRPSPFDLFIRKSPTITCLVVDLAPSKGTVQLTWSRASGKPVNHSTRKEEKQRNGTLTVTSTLPVGT
RDWIEGETYQCRVTHPHLPRALMRSTTKTSGPRAAPEVYAFATPEWPGSRDKRTLACLIQNFMPEDISV
QWLHNEVQLPDARHSTTQPRKTKGSGFFVFSRLEVTRAEWEQKDEFICRAVHEAASPSQTVQRAVSVNP
GKPVATMVSKGEELFTGVVPILVELDGDVNGHKFSVSGEGEGDATYGKLTLKFICTTGKLPVPWPTLVT
TLTYGVQCFSRYPDHMKQHDFFKSAMPEGYVQERTIFFKDDGNYKTRAEVKFEGDTLVNRIELKGIDFK
EDGNILGHKLEYNYNSHNVYIMADKQKNGIKVNFKIRHNIEDGSVQLADHYQQNTPIGDGPVLLPDNHY
LSTQSALSKDPNEKRDHMVLLEFVTAAGI

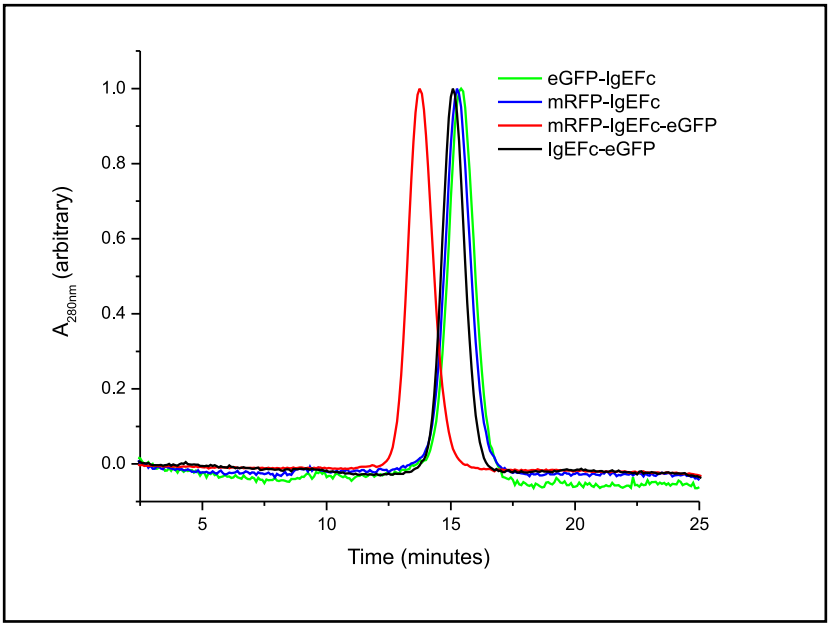

Supplemental Figure S2

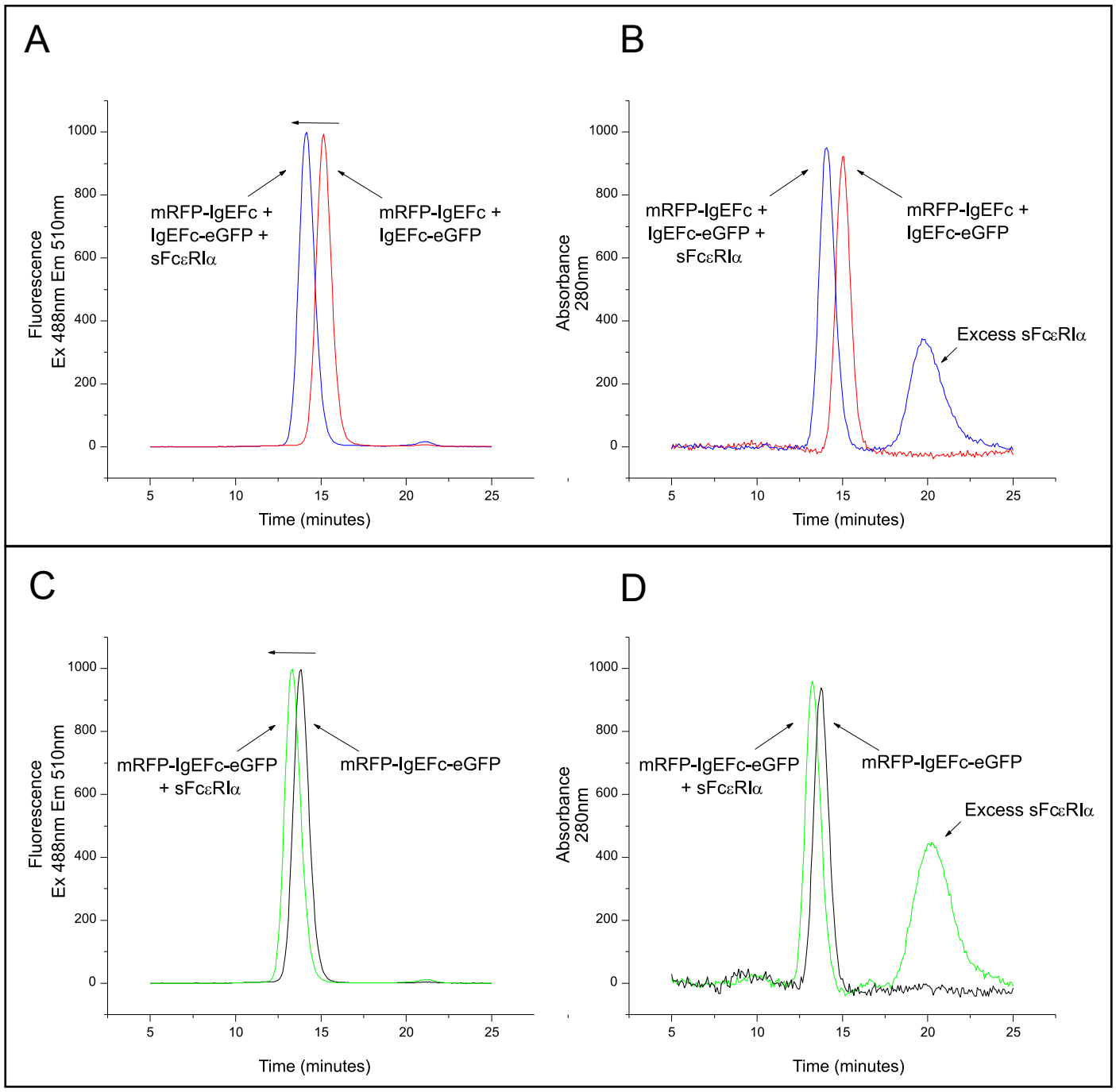

Supplemental Figure S3

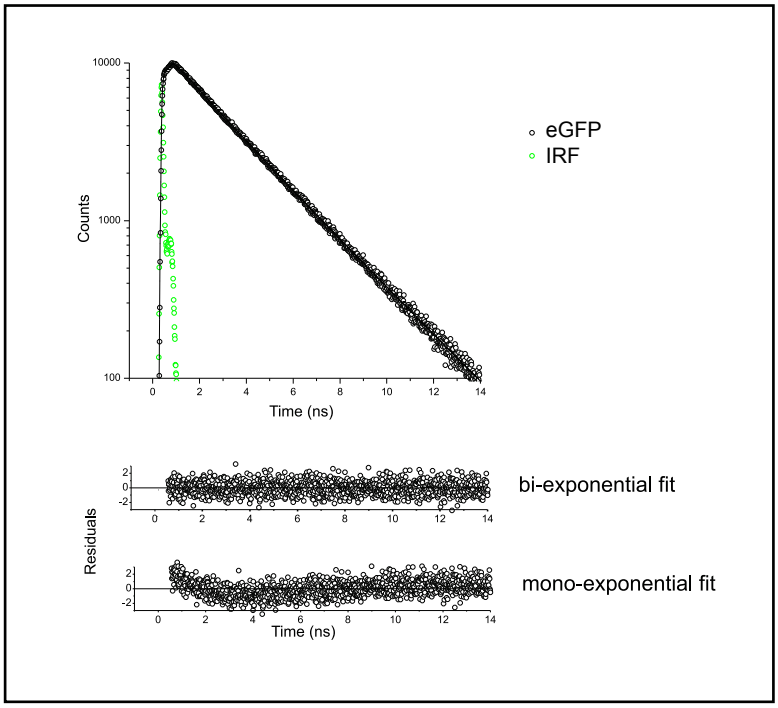

Supplemental Figure S4

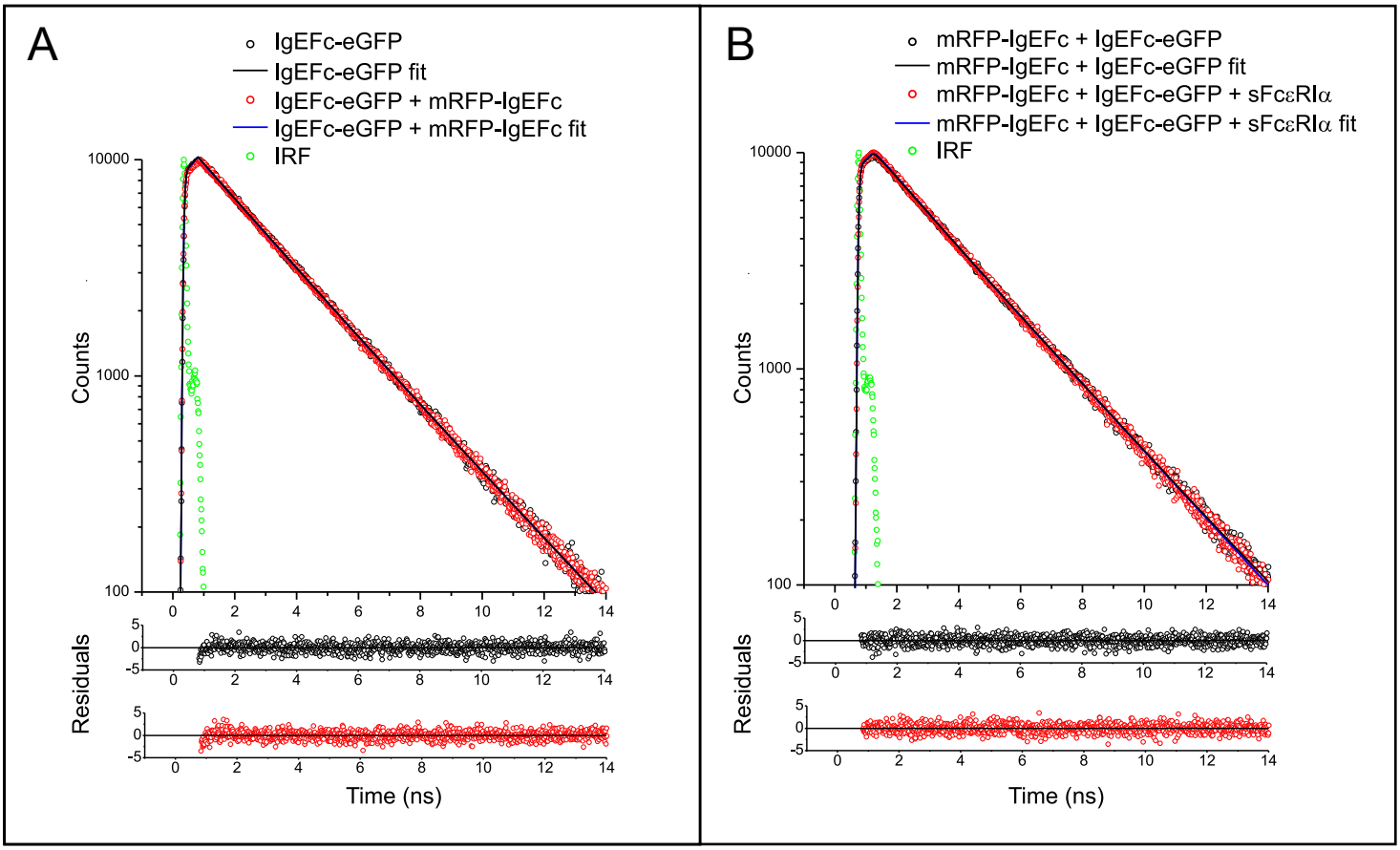

Supplemental Figure S5

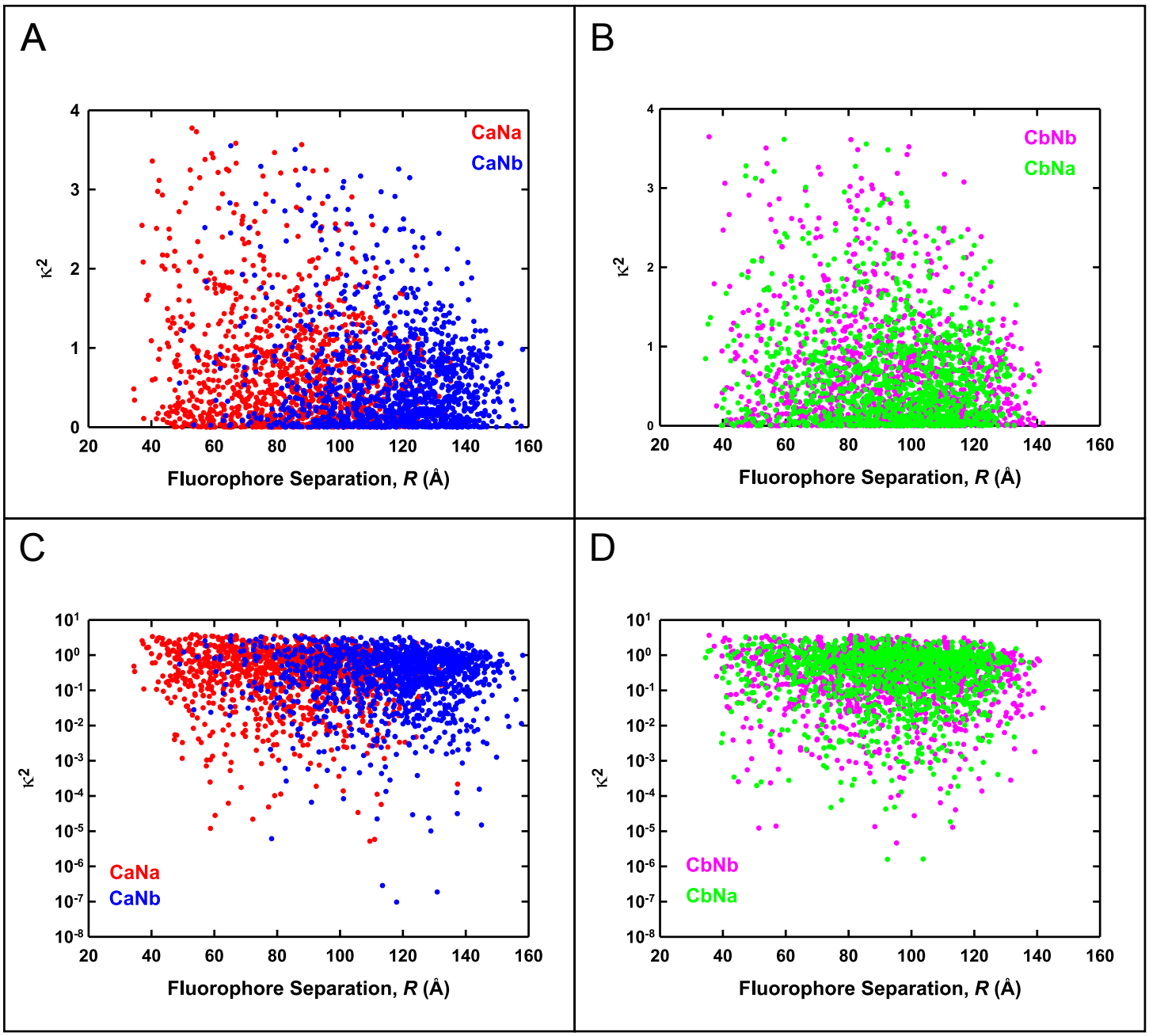

Supplemental Figure S6

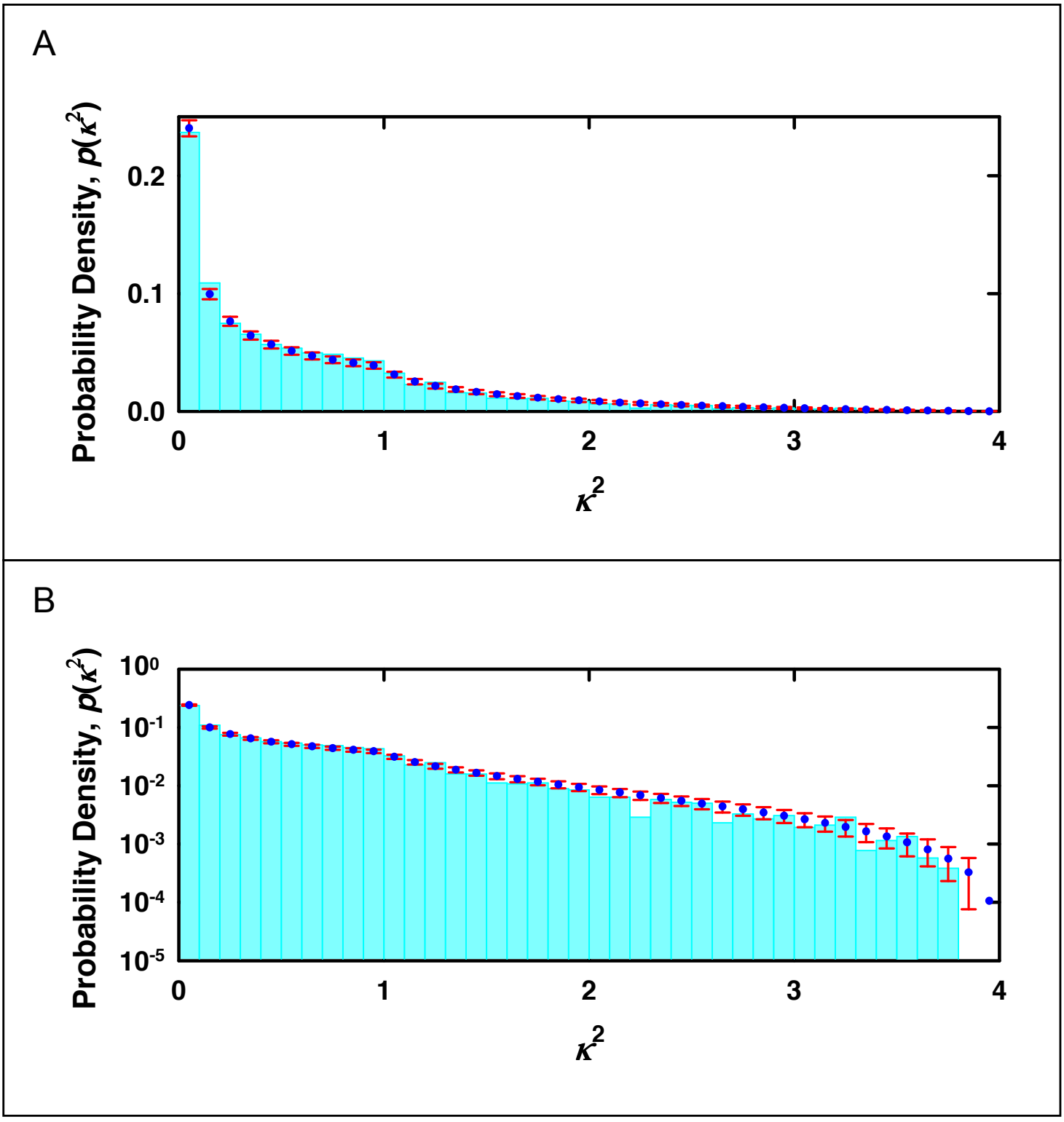

Supplemental Figure S7

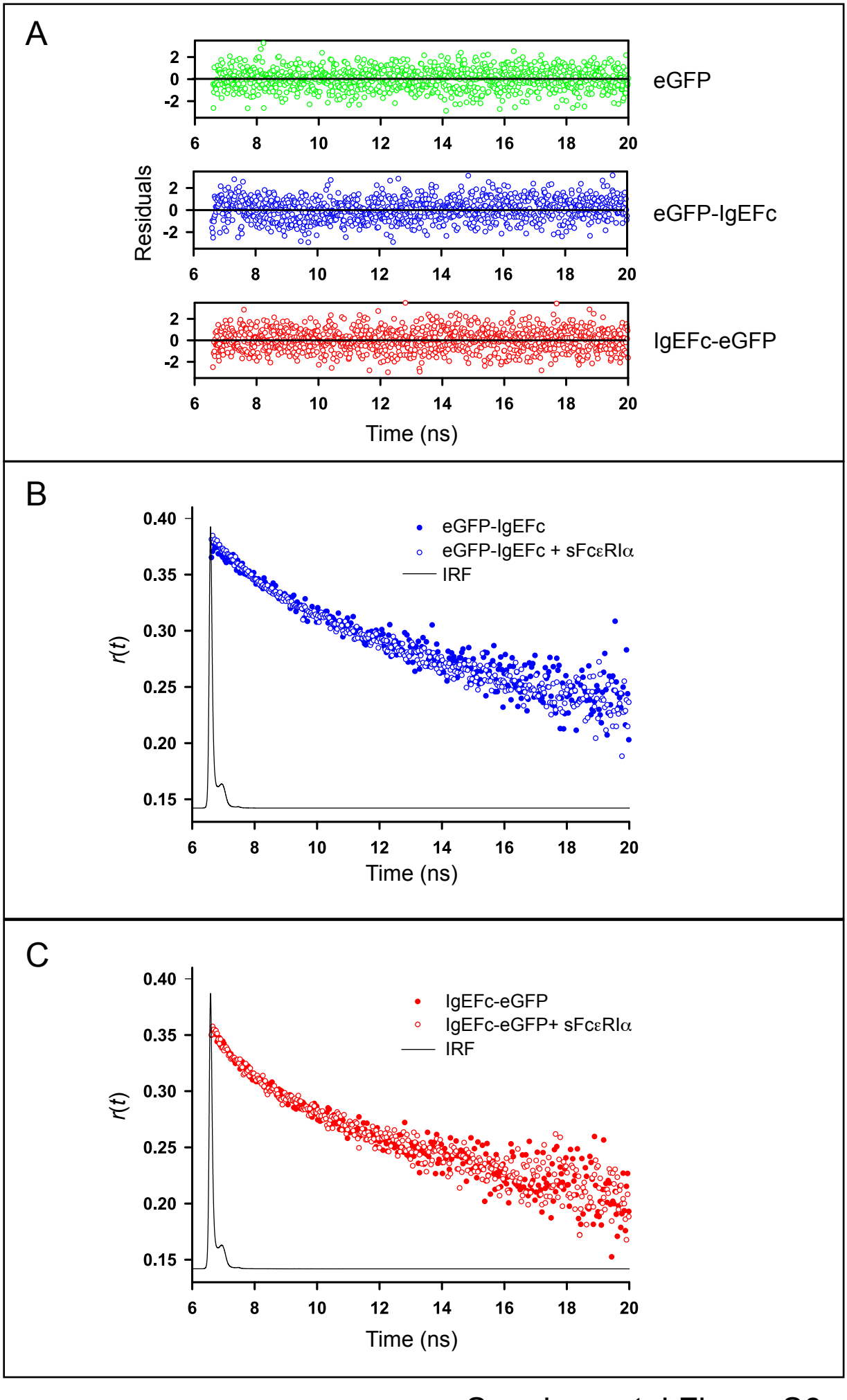

Supplemental Figure S8

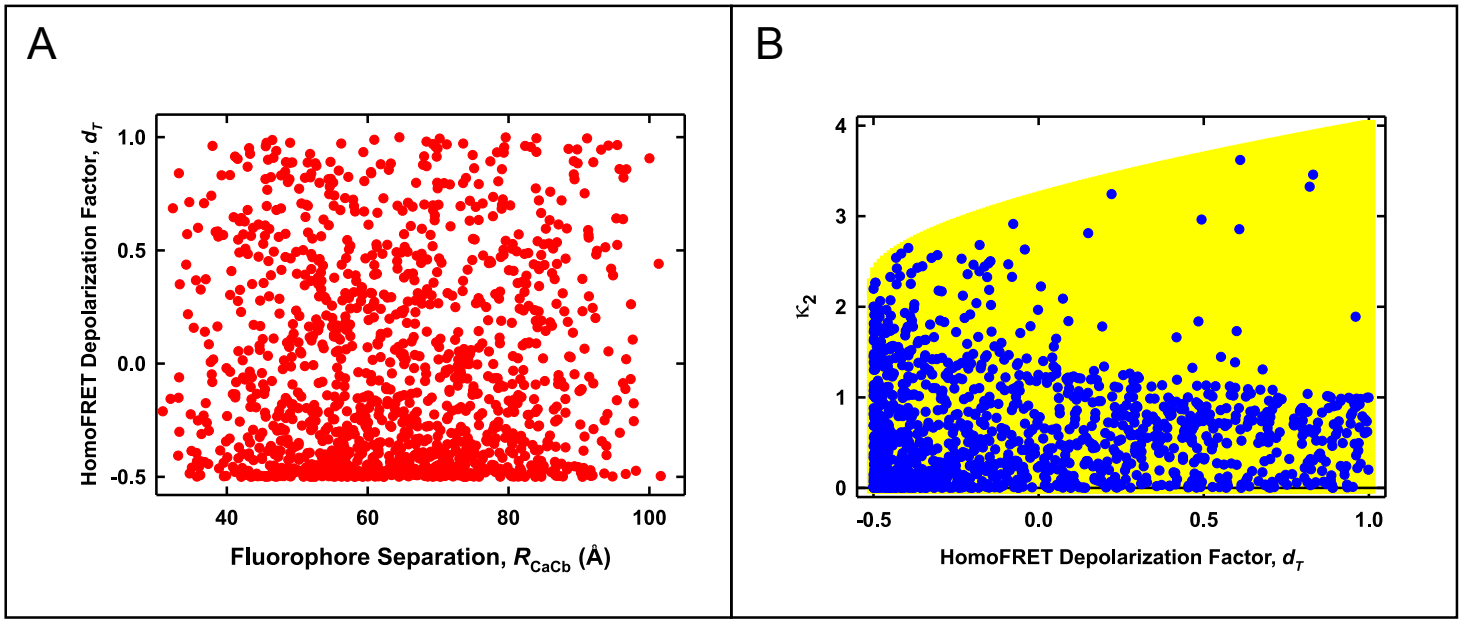

Supplemental Figure S9

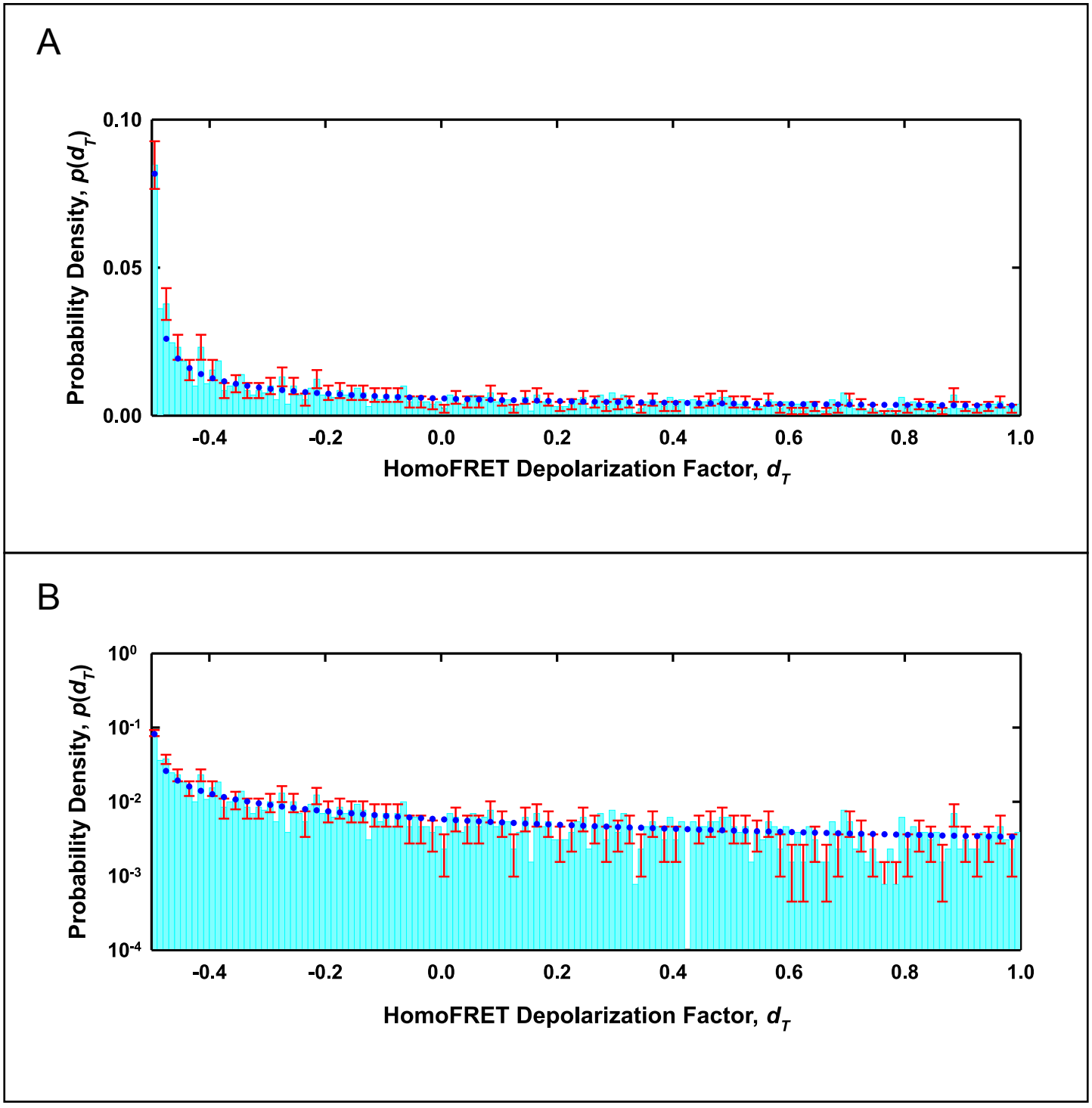

Supplemental Figure S10

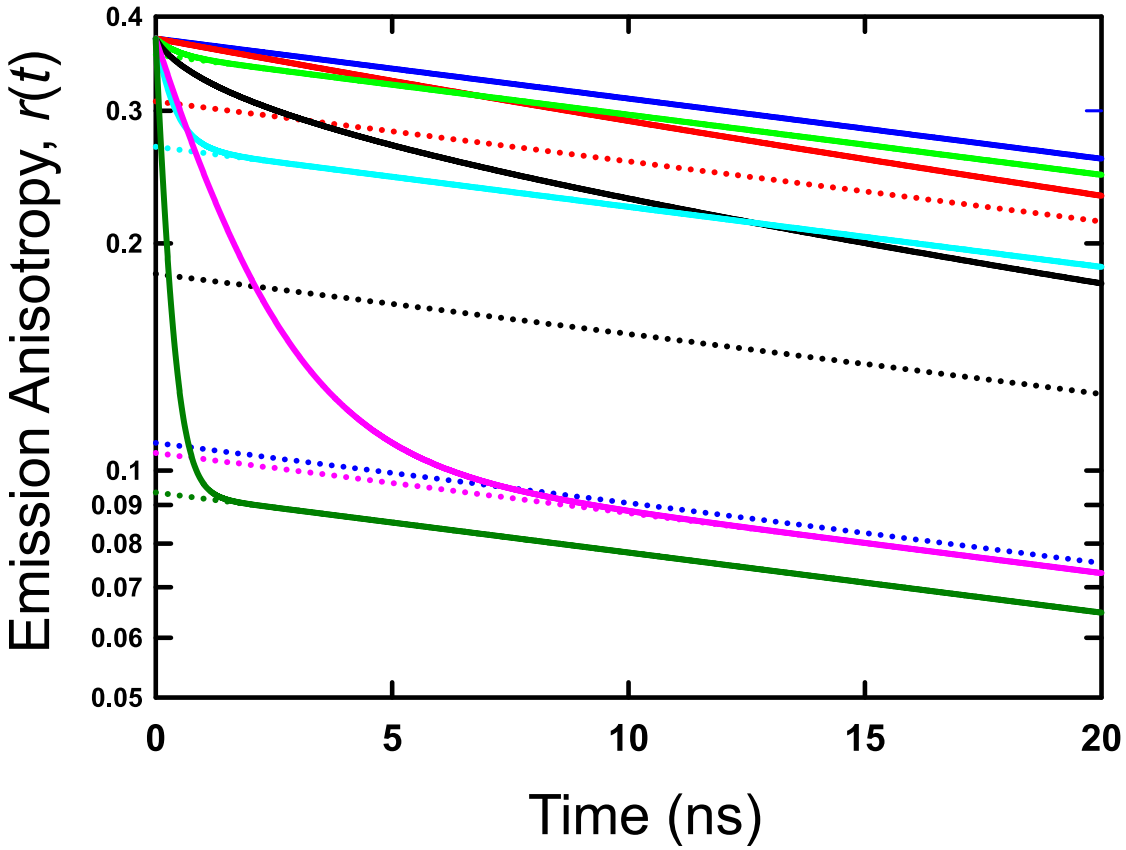

Supplemental Figure S11